TU Delft

Delft University of Technology

Smoothed embedded finite-volume method (sEFVM) for modeling contact mechanics in deformable faulted and fractured porous media

Shokrollahzadeh Behbahani, Sara; Hajibeygi, Hadi; Voskov, Denis; Jansen, Jan Dirk

DOI
10.1016/j.jcp.2022.111143

Publication date
2022

Document Version
Final published version

Published in
Journal of Computational Physics

Citation (APA)
Shokrollahzadeh Behbahani, S., Hajibeygi, H., Voskov, D., & Jansen, J. D. (2022). Smoothed embedded finite-volume method (sEFVM) for modeling contact mechanics in deformable faulted and fractured porous media. *Journal of Computational Physics*, *459*, Article 111143. https://doi.org/10.1016/j.jcp.2022.111143

Important note
To cite this publication, please use the final published version (if applicable).
Please check the document version above.

Copyright
Other than for strictly personal use, it is not permitted to download, forward or distribute the text or part of it, without the consent of the author(s) and/or copyright holder(s), unless the work is under an open content license such as Creative Commons.

Takedown policy
Please contact us and provide details if you believe this document breaches copyrights.
We will remove access to the work immediately and investigate your claim.

This work is downloaded from Delft University of Technology.
For technical reasons the number of authors shown on this cover page is limited to a maximum of 10.

Journal of Computational Physics 459 (2022) 111143

Contents lists available at ScienceDirect

Journal of Computational Physics

www.elsevier.com/locate/jcp

Smoothed embedded finite-volume method (sEFVM) for modeling contact mechanics in deformable faulted and fractured porous media

Sara Shokrollahzadeh Behbahani, Hadi Hajibeygi *, Denis Voskov, Jan Dirk Jansen

Department of Geoscience and Engineering, Faculty of Civil Engineering and Geosciences, Delft University of Technology, Stevinweg 1, 2628 CN Delft, the Netherlands

ARTICLE INFO

Article history:
Received 13 July 2021
Received in revised form 17 January 2022
Accepted 8 March 2022
Available online 15 March 2022

Keywords:
Embedded finite volume method
Fractured and faulted porous media
Fault slip
Coulomb friction law
Reservoir geomechanics
Enhanced finite volume method

ABSTRACT

A smoothed embedded finite-volume modeling (sEFVM) method is presented for faulted and fractured heterogeneous poroelastic media. The method casts a fully coupled strategy to treat the coupling between fault slip mechanics, deformation mechanics, and fluid flow equations. This ensures the stability and consistency of the simulation results, especially, as the fault slip is implicitly found through an iterative prediction-correction procedure. The computational grid is generated independently for embedded faults and rock matrix. The efficiency is further enhanced by extending the finite-volume discrete space by introducing only one degree of freedom per fault element. The embedded approach can lead to an oscillatory stress field at the fault, which damages the robustness of the implicit slip detection strategy. To resolve this challenge, a smoothed embedded strategy is devised, in which the stress and slip profiles are post processed within the iterative loops by fitting the best curve based on a least-square error criterion. The sEFVM provides locally conservative mass flux and stress fields, on staggered grid. Its performance is further investigated for several proof-of-the-concept test cases, including a multiple fault system in a heterogeneous domain. Results indicate that the method develops a promising approach for field-scale relevant simulation of induced seismicity.

© 2022 The Author(s). Published by Elsevier Inc. This is an open access article under the CC BY-NC-ND license (http://creativecommons.org/licenses/by-nc-nd/4.0/).

1. Introduction

Computational geomechanics has been a focal point of research in the past decade, due to its critical role in production optimization and safety assessments [1,2]. Examples can be found, e.g., in studies related to hydraulic fracking [3], quantification of surface subsidence [4], geothermal energy extraction [5], CO_2 sequestration [6], hydrogen energy storage [7–9], and, importantly, induced seismicity [10].

Induced seismic events are earthquakes caused by human activity that alter subsurface stresses. It has been shown that hydrocarbon gas production correlates with induced tremors, especially in depleting gas fields. The Groningen field in the Netherlands is a well known example for induced seismicity [11]. The tremors have remained small on the Richter scale, but they pose risks that prevent further utilization of subsurface capacity for energy and climate relevant projects. Production

* Corresponding author.
E-mail addresses: s.shokrollahzadehbehbahani@tudelft.nl (S. Shokrollahzadeh Behbahani), h.hajibeygi@tudelft.nl (H. Hajibeygi), d.v.voskov@tudelft.nl (D. Voskov), j.d.jansen@tudelft.nl (J.D. Jansen).

https://doi.org/10.1016/j.jcp.2022.111143
0021-9991/© 2022 The Author(s). Published by Elsevier Inc. This is an open access article under the CC BY-NC-ND license (http://creativecommons.org/licenses/by-nc-nd/4.0/).

from the field has been throttled back since 2013 and is coming to a full shut-down by mid-2022 to curtail future events [12]. But field shut-down does not necessarily guarantee the immediate prevention of future seismic events. In fact, the underground stress stabilization occurs through a slow time-dependent process, during which fault activation (perhaps with lower magnitudes) can potentially take place. This emphasizes the need to look beyond field shut-down and to develop robust strategies to minimize future risks. To achieve this goal, it is essential to understand the mechanisms that lead to such unfavorable situations via modeling and simulation.

Numerical models for induced seismicity have evolved over the years. The earliest models for geo-systems proposed loosely coupled flow dynamics and mechanics [13,14]. Later, iterative or sequentially coupled [15] and fully coupled methods [16] emerged. These incorporate the effects of geomechanical deformation on flow parameters (such as permeability and porosity) and vice versa (e.g., the effect of pressure on fault stability). Fully-coupled approaches add to the computational costs, but extend the simulation stability compared with their loosely-coupled predecessors [15,17].

Fault stability was initially modeled based on a simple Coulomb failure criterion [18]. This model correlates the normal stress on the fault with a maximum threshold, beyond which the fault slips [19]. More realistic quasi-static and dynamic friction models were later developed by incorporating more complex physics of fault re-activation. These include slip weakening or strengthening models [20,21], rate and state models [22–24] and more recently the CNS model [25–27]. Dynamic frictional fault slip models are used to capture more complex behavior. In these models, parameters such as energy dissipation rate, damage potential, slip velocity, slip duration and thermal weakening effects are considered [28]. These models do well in characterizing laboratory friction experiments, but challenges still remain in scaling up the results to make them relevant for real-field natural fault systems [29].

The choice of the numerical discretization approach for the faulted poroelastic system, be it finite volumes (FVM) [30–32], elements (FEM) [33], or differences (FDM) [34,32], is not an obvious one [35]. Given that each offer problem-specific advantages, all have been adapted individually, or in combination with each other for flow and mechanics. FDM has been the earliest discretization scheme, due to its simplicity and convenience for structured grids. One motivation behind the development of newer integral-based discretization techniques (FVM and FEM) is the limitation of FDM in handling complex geometries especially in multiple dimensions [36]. FEM was originally developed for static stress analysis but expanded well beyond its scope. It remains the most widely used method in computational mechanics. This is in part due to its versatility in handling highly heterogeneous, geometrically intricate domains with irregular boundaries [37]. Furthermore, FEM is efficient for the implementation of material and geometric nonlinearities [38]. However FEM is the second best option for flow modeling after FVM. This is because FVM is locally conservative at the discrete level [39]. FVM has the combined advantage of FDM in being relatively simple to implement, and FEM in having flexibility towards complex geometries.

Initially, the computational mesh used to capturing the geological domain was always a structured mesh, imposed on the heterogeneous geological field. Later unstructured meshes were also utilized to capture discontinuities (e.g. faults and fractures) by confining them at grid interfaces. However, for complex geometries, this representation often becomes overly detailed making subsequent calculations impractical [40–44].

The computational mesh for modeling poroelasticity using FVM can consist of collocated [45] or staggered grids for the two unknowns of pressure and displacement. Note that local conservation is guaranteed on the corresponding control volumes developed for each term (here, stress and mass flux). As such, using staggered grids allows for strictly conservative mass flux and stress field on the overlapping staggered mesh [34,32,46,47].

Embedded methods use appropriate relationships to link the fault network to the matrix with minimal mesh complexities [48–51]. The embedded framework has been used with both FEM (e.g. XFEM [52–54]) and FVM with sequentially-coupled [55,56] and fully-coupled [57] flow-mechanics simulations. A benchmark study was performed to compare the quality of the embedded-structured and conforming-unstructured mesh approaches for single-phase flow in porous media [58].

Recently, the embedded FVM (EFVM) method has been successfully proposed for determining pressure and displacements in a faulted system under pore pressure variations. Flow and mechanics were loosely coupled using a sequential coupling approach based on a fixed-stress scheme [55,56]. Later, the computational efficiency and condition number of EFVM was compared to XFEM [59]. This showed EFVM is much faster in terms of CPU time, but has a higher condition number. There are two reasons for this. First, for each direction, there is one additional unknown per cell in EFVM, whereas there are at least four in XFEM. Second, EFVM integrals are found analytically, while XFEM uses numerical integration.

Despite the recent progress in the EFVM method, major challenges remain for reliable simulation of fault re-activation in the context of induced seismicity. The first of these is the incorporation of fault slip as a fully-implicit fully-coupled process with direct functionality of pore pressure and deformation. This plays an essential role when the geologic setting exhibits a strong physical association of mechanics with flow, such as in the case of production from faulted gas reservoirs [60]. A weak or sequential coupling may potentially result in conditionally stable results for multi-physics problems [15] or becomes more expensive in terms of CPU performance [61].

The second challenge is the accurate calculation of the stresses affecting faults. These stresses are fundamental in identifying the stick-slip situation and quantifying the correct value of slip. But an element of nonlinearity arises due to the inter-dependence of slip on post-processed stresses. This requires iterations to ensure the estimated fault slip remains in agreement with the most recent stress field.

The third challenge concerns the occurrence of oscillations in the stress and slip profiles of the faults, as has been observed in previous EFVM results [55,56]. These oscillations arise due to the embedded nature of EFVM, primarily when

faults are misaligned with the matrix mesh. While the embedded framework is quite convenient for heavily-faulted systems [62], these oscillations pose a substantial hindrance to the stability of the implicit EFVM method.

In this study, we resolve these challenges by introducing a fully-implicit fully-coupled smoothed embedded finite volume method (sEFVM) for modeling poroelastic deformation and fault slip. The framework supports heterogeneous properties for rock and faults. This work contains a series of improvements to an already existing EFVM framework. We report on the oscillation in the stress and slip profiles across faults as a side-effect of the embedded fault representation. We evaluate the consequences of these oscillations in our study on fault re-activation, and suggest means to handle them. This ensures a smooth scheme that we call smoothed EFVM (sEFVM). Furthermore, we introduce an iterative strategy to obtain the fault slip implicitly fully-coupled together with the pore pressure and rock deformation. We provide numerical test cases to evaluate the order of accuracy of FVM and EFVM methods. We test our poroelastic simulator with analytical solutions and compare poroelastic deformation to mechanics-only solutions. A heavily-faulted poroelastic system is studied to investigate the capacity of the sEFVM method.

The paper is structured as follows. Next, the governing equations for the sEFVM method are introduced, followed by numerical test cases. These test cases include consistency analyses of FVM for poromechanics simulations, for synthetic and well-established test cases. Then, faults are introduced which follow Mohr-Coulomb friction law. To this end, numerical solutions of sEFVM for faulted media are validated against analytical ones, and then benchmarked against another simulator. Furthermore, to demonstrate its applicability, the sEFVM is applied to model deformation and fault slip in a heavily faulted heterogeneous medium. We highlight the steps forward made by development of sEFVM compared with the existing EFVM approaches, especially on consistent identification of the fault slips and smooth solution fields. Finally, concluding remarks are presented.

2. Governing equations

The single-phase mass conservation equations for a slightly-compressible poroelastic domain and flow-conductive fractures and faults based on the embedded discrete fracture modeling (EDFM) approach read [50,48],

$$b\frac{\partial \nabla\cdot\vec{u}}{\partial t}+\frac{1}{M}\frac{\partial p_m}{\partial t}+\nabla\cdot\left(-\frac{k_m}{\mu}\cdot\nabla p_m\right)+\Psi_{m\to f}=Q_m, \tag{1}$$

and

$$\frac{\partial E_f}{\partial t}+\nabla\cdot\left(-\frac{ak_f}{\mu}\cdot\nabla p_f\right)+\Psi_{f\to m}=Q_f, \tag{2}$$

where b is the Biot coefficient, $\vec{u}$ is matrix deformation, t is time, M is the Biot modulus, p is pressure, k is permeability, μ is phase viscosity, Ψ is the net flux exchanged between the matrix and fracture/fault, Q is the source term, a is fracture/fault aperture and E^f is the total accumulation in the fracture/fault. Subscripts m and f stand for the matrix and fault/fracture, respectively.

The term E^f becomes negligible if the change in the aperture (e.g. dilation) and porosity of flow-conductive faults and fractures (ϕ_f) is neglected, because

$$\frac{\partial E_f}{\partial t}=\left[\frac{1}{\rho}\frac{\partial}{\partial t}(a\rho\phi_f)\right]\approx\frac{\partial}{\partial t}(a\phi_f). \tag{3}$$

Note that one can include dilation due to slip to further model the void aperture E_f term [63].

The linear momentum balance for a poroelastic domain with faults and fractures can be stated as

$$\nabla\cdot(\widetilde{\sigma}-bp\widetilde{I})+\vec{f}=0, \tag{4}$$

where $\widetilde{\sigma}$ is the effective stress tensor, $\widetilde{I}$ is the identity matrix and $\vec{f}$ is the body force per unit volume [64]. Assuming linear elastic deformation [64], stress is linearly proportional to the displacement gradient, i.e.,

$$\widetilde{\sigma}=\widetilde{C}:\nabla^s\vec{u}, \tag{5}$$

where ∇^s is the symmetric gradient operator and $\widetilde{C}$ is the elasticity tensor consisting of elasticity parameters [64].

Fault slip occurs when the tangential stresses on the fault, i.e., τ, surpass the maximum threshold value, i.e., τ^{max}. Here, the Coulomb/Byerlee friction law [18] is applied to quantify τ^{max} as

$$\tau^{max}=|\mu_c+\mu_f\cdot\sigma_n|. \tag{6}$$

Here, μ_f is the friction coefficient, μ_c is the cohesive force of the contact, and σ_n is the normal stress on the fault. Where not mentioned in this study, the value of μ_c is taken as zero. The governing equations above subject to proper initial and boundary conditions for both flow and mechanics form a well-posed system of equations. These conditions in general form can be expressed as

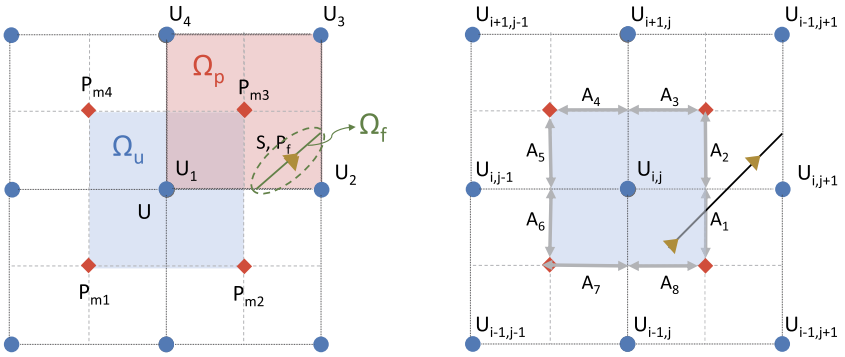

Fig. 1. Control volumes and numbering scheme for displacement and matrix pressure (left) and integration surfaces for mechanical control volume (right).

$$\text{Prescribed boundary displacement:} \quad \vec{u} = \vec{u}_{\partial\Omega_{u,D}} \tag{7a}$$

$$\text{Prescribed boundary total stress:} \quad (\widetilde{C} : \nabla^s \vec{u} - bp\widetilde{I}) \cdot \vec{n}_{\partial\Omega_{u,N}} = \vec{f} \tag{7b}$$

$$\text{Prescribed boundary pore pressure:} \quad p = p_{\partial\Omega_{p,d}} \tag{7c}$$

$$\text{Prescribed boundary flux:} \quad -(\frac{k_m}{\mu} \cdot \nabla p) \cdot \vec{n}_{\partial\Omega_{p,N}} = q \tag{7d}$$

$$\text{Initial pressure:} \quad p_{\Omega_p} = p_{\Omega_p}(t=0) \tag{7e}$$

$$\text{Initial displacement:} \quad \vec{u}_{\Omega_u} = \vec{u}_{\Omega_u}(t=0) \tag{7f}$$

Here, $\vec{n}$ is the unit normal vector to the corresponding boundaries of flow and mechanics. In addition, sub-indices $\bullet_{,D}$ and $\bullet_{,N}$ indicate the part of the displacement and pressure domain boundaries ($\bullet \in \{\partial\Omega_p, \partial\Omega_u\}$) in which Dirichlet (D) and Neumann (N) boundary conditions are imposed. Note that the union of the Dirichlet and Neumann boundary interfaces form the entire domain boundary, i.e., $\Omega_{p,D} \cup \Omega_{p,N} = \Omega_p$ and $\Omega_{u,D} \cup \Omega_{u,N} = \Omega_u$.

3. Method

We use the finite volume method (FVM) on staggered structured grids for both flow and mechanics. In this approach, the equations are integrated over corresponding control volumes for mechanics (Ω_u) and flow (Ω_p) shown in Fig. 1. For flow inside a faulted poroelastic rock matrix, Eq. (1) is integrated over the control volume for flow inside the matrix (Ω_p) as

$$b \int_{\partial\Omega_p} \frac{\partial \vec{u}}{\partial t} \cdot \vec{n}\, dS + \int_{\Omega_p} \frac{1}{M} \frac{\partial p_m}{\partial t}\, dV - \int_{\partial\Omega_p} \frac{k_m}{\mu} \cdot \nabla p_m \cdot \vec{n}\, dS + \int_{\Omega_p} \Psi_{m\to f}\, dV = \int_{\Omega_p} Q_m\, dV. \tag{8}$$

Faults are represented with a lower dimension than the matrix grid. Slip (s) and fault pressure (p_f) unknowns are located on the embedded fault. Clearly, the mesh for the reservoir and faults and fractures are completely independent. For flow inside the fault, Eq. (2) is integrated over the displacement control volume of the fault, i.e. Ω_f, as

$$\int_{\Omega_f} \frac{\partial E_f}{\partial t}\, dS - \int_{\partial\Omega_f} \frac{ak_f}{\mu} \cdot \nabla p_f \cdot \vec{n}\, dl = \int_{\Omega_f} \Psi_{f\to m}\, dS + \int_{\Omega_f} Q_f\, dS. \tag{9}$$

In these equations, the net flux leaving the matrix to the fracture/fault domain is identified by $\Psi_{m\to f}$ [50], which is defined as

$$\Psi_{m\to f} = \eta \frac{k_m}{\mu} \frac{p_f - p_m}{V}. \tag{10}$$

Similarly, $\Psi_{f\to m}$ indicates the flux leaving fracture/fault to matrix, i.e.,

$$\Psi_{f\to m} = \eta \frac{k_m}{\mu} \frac{p_m - p_f}{A}. \tag{11}$$

Here, V and A are volume of matrix element and area of the overlapping fault cell. Moreover, η is the connectivity index between matrix and fault/fracture. For matrix cell (i, j) and fracture element k, it is defined as

$$\eta_{ij,k} = \frac{A_{ij,k}}{\langle d \rangle_{ij,k}}, \tag{12}$$

where $A_{ij,k}$ is the area fraction of the fracture element inside the matrix cell and $\langle d \rangle_{ij,k}$ is the average distance of point inside the cell to the fracture segment. More details on EDFM and its most updated formulations can be found in the literature [50,62].

For mechanics, Eq. (4) is integrated over control volume Ω_u as

$$\int_{\Omega_u} \nabla \cdot \left(\widetilde{C} : \nabla^s \vec{u} - bp\widetilde{I} \right) dV = \int_{\Omega_u} \vec{f}\, dV. \tag{13}$$

According to the divergence theorem [65], this integral is restated as

$$\int_{\partial\Omega_u} (\widetilde{C} : \nabla^s \vec{u}) \cdot \vec{m}_{\Omega_u}\, dS - b \left(\int_{\partial\Omega_u} p\, dS \right) \widetilde{I} = \int_{\Omega_u} \vec{f}\, dV, \tag{14}$$

where, $\partial\Omega_u$ is the boundary of the displacement control volume, which consists of 8 segments for each cell named A_1 to A_8 as shown in Fig. 1).

The effective stress tensor is defined as

$$\widetilde{\sigma} = \begin{pmatrix} \sigma_{xx} & \sigma_{xy} \\ \sigma_{yx} & \sigma_{yy} \end{pmatrix}, \tag{15}$$

and by incorporating this definition into Eq. (14) we obtain

$$\int_{\partial\Omega_u} (\sigma_{xx} - bp)\, dy + \int_{\partial\Omega_u} \sigma_{xy}\, dx + \int_{\Omega_u} f_x\, dV = 0, \tag{16a}$$

$$\int_{\partial\Omega_u} (\sigma_{yy} - bp)\, dx + \int_{\partial\Omega_u} \sigma_{yx}\, dy + \int_{\Omega_u} f_y\, dV = 0, \tag{16b}$$

for structured grids. Using the linear elasticity theory based on the first (λ) and second (G) Lame parameters, components of $\widetilde{\sigma}$ are

$$\sigma_{xx} = (\lambda + 2G) \frac{\partial u_x}{\partial x} + \lambda \frac{\partial u_y}{\partial y}, \tag{17a}$$

$$\sigma_{yy} = (\lambda + 2G) \frac{\partial u_y}{\partial y} + \lambda \frac{\partial u_x}{\partial x}, \tag{17b}$$

$$\sigma_{xy} = \sigma_{yx} = G \left(\frac{\partial u_x}{\partial y} + \frac{\partial u_y}{\partial x} \right). \tag{17c}$$

The elasticity parameters (λ) and (G) are assigned to mechanical control volumes (i.e. Ω_u). They can constitute a heterogeneous map over the domain.

If Eq. (17) is placed in Eq. (16), the momentum balance reads

$$\int_{d\Omega_u} \left((\lambda + 2G) \frac{\partial u_x}{\partial x} + \lambda \frac{\partial u_y}{\partial y} - bp_m \right) dy + \int_{d\Omega_u} G \left(\frac{\partial u_x}{\partial y} + \frac{\partial u_y}{\partial x} \right) dx = -\int_{\Omega_u} f_x\, dV, \tag{18a}$$

$$\int_{d\Omega_u} \left((\lambda + 2G) \frac{\partial u_y}{\partial y} + \lambda \frac{\partial u_x}{\partial x} - bp_m \right) dx + \int_{d\Omega_u} G \left(\frac{\partial u_x}{\partial y} + \frac{\partial u_y}{\partial x} \right) dy = -\int_{\Omega_u} f_y\, dV. \tag{18b}$$

These equations can be quantified based on the integrals of derivatives of displacement. The displacement field is discontinuous when slip occurs. To capture this discontinuity it was suggested to append the regular, continuous part of displacement with a jump [66]. Based on this approach the appended displacement field is

$$\vec{u} \approx \sum_{i=1}^{4} N_i \vec{u}_i + \sum_{i=1}^{n_s} s_i W_i \vec{t}_i, \tag{19}$$

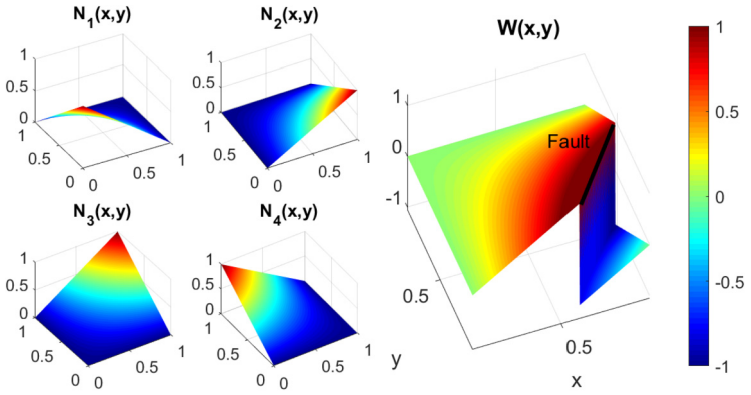

Fig. 2. Illustration of basis functions and the W function used in the EFVM method. (For interpretation of the colors in the figure(s), the reader is referred to the web version of this article.)

where s is slip. N are bi-linear FVM basis functions that interpolate displacement at local coordinates of (x, y) inside a block of dimensions Δx by Δy. These are

$$N_1(x,y) = \left(1 - \frac{x}{\Delta x}\right)\left(1 - \frac{y}{\Delta y}\right), \tag{20a}$$

$$N_2(x,y) = \left(\frac{x}{\Delta x}\right)\left(1 - \frac{y}{\Delta y}\right), \tag{20b}$$

$$N_3(x,y) = \left(\frac{x}{\Delta x}\right)\left(\frac{y}{\Delta y}\right), \tag{20c}$$

$$N_4(x,y) = \left(1 - \frac{x}{\Delta x}\right)\left(\frac{y}{\Delta y}\right). \tag{20d}$$

The numbering from 1 to 4 refers to corners of a square grid counted counter-clockwise beginning from the bottom-left as shown in Fig. 1 for displacements.

For cells intersected by faults, the latter part of Eq. (19) is included. This term consists of tangential slip (s), directional component of the unit tangent vector to the fault ($\vec{t}$), and function W defined as

$$W(x,y) = \sum_{i=1}^{4} N_i(x,y)\left[H\Big(f(x,y)\Big) - H\Big(f(x_i,y_i)\Big)\right], \tag{21}$$

where H is a modified Heaviside function defined as

$$H(\zeta) = \begin{cases} -1 & \zeta \le 0 \\ +1 & \zeta > 0 \end{cases}. \tag{22}$$

In Eq. (21), $f(x, y)$ is the signed distance from the fault. Depending on which side of the fault a point is located, it will be positive or negative. The Heaviside value of $f(x, y)$ will be +1 or -1. This introduces the discontinuity into the model which is used to calculate the tangential slip. It is noted that the current framework allows for definition of a single fault node per matrix grid cell.

Fig. 2 shows a plot of FVM basis functions and $W(x, y)$ over a unit square grid. This image shows that displacement is linearly interpolated inside each grid. In the case of a faulted grid, there is a jump at the location of the fault.

The chosen form for Eq. (19) gives the EFVM method advantages. First, the simplicity of the bi-linear basis functions allows for analytical determination of the integrals in Eq. (18). Here, the derivatives of the displacement are calculated analytically, and then integrated over the control volume surfaces of the structured grid considered in Fig. 1. An example of this is given in the Appendix. Second, the total displacement function of Eq. (19) includes the slip. So slip is calculated directly as an independent variable at the fault location and is not determined as a post-processed estimate. Furthermore, EFVM can be used with embedded fracture/fault models for flow with the least amount of complexity.

Next, the friction law (Eq. (6)) is considered for the fault. Based on the τ^{max} obtained from friction law, the following is implemented based on the local shear stress for node i along the fault j (i.e. $\tau_{i,j}$):

$$\tau_{i,j} = \begin{cases} \tau_{i,j} & \tau_{i,j} < \tau_{i,j}^{max} \\ \tau_{i,j}^{max} & \tau_{i,j} \ge \tau_{i,j}^{max} \end{cases}. \tag{23}$$

In Equation (23), the shear stress (τ) is compared to τ^{max}, which depends on the normal stress (σ_n). These stresses are found by projection of the effective stress tensor onto the fault. This is done via defining the traction vector $\vec{T}$ as

$$\vec{T} = \widetilde{\sigma} \cdot \vec{n}. \tag{24}$$

Here, $\vec{n} = n_x\vec{i} + n_y\vec{j}$ is the unit normal vector to the fault. Then, the normal and tangential stress components on the fault can be found via

$$\sigma_n = \vec{T} \cdot \vec{n}, \tag{25a}$$

$$\tau = \vec{T} \cdot \vec{t} \tag{25b}$$

operations. Here, $\vec{t}$ is the unit tangential vector to the fault. Given that this vector is normal to $\vec{n}$, it has components $\vec{t} = n_y\vec{i} - n_x\vec{j}$. It is noted that the vector form for these stresses is used to represent the vector of scalar values of normal and tangential stresses along the nodes of the fault.

Eq. 25 can be used to express the stresses at the fault location as

$$\sigma_n = (\lambda + 2Gn_x^2)\frac{\partial u_x}{\partial x} + (\lambda + 2Gn_y^2)\frac{\partial u_y}{\partial y} + 2Gn_xn_y\left(\frac{\partial u_x}{\partial y} + \frac{\partial u_y}{\partial x}\right), \tag{26a}$$

$$\tau = 2Gn_xn_y\frac{\partial u_x}{\partial x} - 2Gn_xn_y\frac{\partial u_y}{\partial y} + G(n_y^2 - n_x^2)\frac{\partial u_y}{\partial x} + G(n_y^2 - n_x^2)\frac{\partial u_x}{\partial y}. \tag{26b}$$

The momentum balance equation for matrix, i.e. Eq. (18), friction law for the fault, i.e. Eq. (26), mass balance equation for the matrix, i.e. Eq. (8), and mass balance equation for the flow-conductive fault, i.e. Eq. (9), are solved together fully-implicitly and fully-coupled for the faulted poroelastic system, i.e.,

$$\begin{bmatrix} J_{uu} & J_{us} & J_{up_m} & J_{up_f} \\ J_{su} & J_{ss} & J_{sp_m} & J_{sp_f} \\ J_{p_mu} & J_{p_ms} & J_{p_mp_m} & J_{p_mp_f} \\ J_{p_fu} & J_{p_fs} & J_{p_fp_m} & J_{p_fp_f} \end{bmatrix} \cdot \begin{bmatrix} u \\ s \\ p_m \\ p_f \end{bmatrix} = \begin{bmatrix} f_u \\ c_s \\ Q_{p_m} \\ Q_{p_f} \end{bmatrix}. \tag{27}$$

The Jacobian matrix entries are identified by $J_{i,j}$, $\forall\{i, j\} \in \{u, s, p_m, p_f\}$. Also note that the slip nodes at which the most-updated estimate of friction is equal or greater than the maximum tolerable friction are included in this system. All other slip nodes, i.e. belonging to stick condition, are excluded in the linear system of Eq. (27).

The procedure of sEFVM for each time step is shown in Algorithm 1. In the first time step, the system of equations is solved using a continuum model (assuming there are no slipping nodes). This predictor-step solution is used as a first estimate for calculating stresses at the faults. The shear stresses along the faults, i.e. τ, are then obtained and compared to the maximum tolerable threshold of τ^{max}, as in Eq. (6), for each fault. New degrees of freedom, i.e. $\vec{n}_s$, are then appended to the system of Eq. (27) only when, and where, the slip criterion is met (i.e. nodes which satisfy $\tau > \tau^{max}$). The new system is solved, stresses are recalculated, slip-stick conditions are re-identified and the procedure is repeated until convergence is reached.

Algorithm 1: Procedure of the sEFVM method at each time step.

Result: $[u_x, u_y, p_m, p_f, s']$
Solve poroelastic continuum model to find $[u_x, u_y, p_m, p_f]^1$; // Initialize
Calculate stresses τ^1 and σ_n^1 ;
Determine frictional threshold $\tau^{max,1}$ using Eq. (6);
Find slipping nodes $\vec{n}_s^1$ where $\tau^1 \geq \tau^{max,1}$;
Set $\xi = 1$ and $\kappa = 1$;
while $\xi \neq 0$ **do** // Begin iterative loop
  Append system of equations with $\vec{n}_s^\kappa$ unknowns for fault slip;
  Solve poroelastic faulted model to find $[u_x, u_y, p_m, p_f, s]^{\kappa+1}$;
  Calculate stresses $\tau^{\kappa+1}$ and $\sigma_n^{\kappa+1}$;
  Find smooth stress profiles $\tau'^{\kappa+1}$ and $\sigma_n'^{\kappa+1}$; // Smoothing of stress
  Determine frictional threshold $\tau^{max,\kappa+1}$ using Eq. (6);
  Find new slipping nodes $\vec{n}_s^{\kappa+1}$ where $\tau'^{\kappa+1} \geq \tau^{max,\kappa+1}$;
  Update ξ, i.e., count of nodes for which stick-slip condition is changed ;
  Assign $(\kappa + 1) \rightarrow \kappa$;
end
Find smooth slip profile s' ; // Smoothing of slip

As numerical examples will show later, oscillations can arise in the fault stress (and slip) profiles of EFVM. These oscillations are an anticipated consequence of the embedded incorporation of faults in the EFVM method, when faults are

misaligned with the matrix grid. An oscillatory stress profile will cause problems because it is used for determining stick-slip conditions. When an oscillatory stress profile is used, the slip-stick condition can fluctuate for a node, preventing the convergence to a consistent slip condition. To resolve this challenge, a smoothing procedure is developed in this study. During iterations, the smoothing domain covers the stress profile for each fault. The fault stress profile has no overlap or gaps. So, a smooth profile is fitted to the original curve. The method for deriving this fit can vary. It is, however, found that the fit to a polynomial works well for all cases studied by the authors. Data fitting to the polynomial is done based on least squares method, which minimizes the summed square of residuals [67].

The smoothed stress is used instead of the oscillatory curve, to find $\vec{n}_s$ again. If the estimates are different, the system is solved with new degrees of freedom for fault slip defined by the updated $\vec{n}_s$ vector. This is repeated until $\vec{n}_s$ remains unchanged. At that point, the procedure moves forward in time. For problems where faults are close to slip, neglecting this iterative step can result in incorrect results (as shown in later examples). For cases far from such conditions (e.g. the fault will clearly slip or remain stationary), the initial assumption is usually correct. For most problems, a single iteration is sufficient, thus the added computational load for the studied cases is found to be insignificant. The small number of iterations is believed to be due to the fact that there is little nonlinearity in the simplified physics of the studied model. The slip profile may also demonstrate oscillations. For this reason, it is smoothed at the last time-step for improved interpretation.

In this study the error ϵ is defined as

$$\epsilon = \frac{\left\| \mathbf{x}_{ref} - \mathbf{x} \right\|_\infty}{\left\| \mathbf{x}^h_{ref} \right\|_\infty}, \tag{28}$$

where x_{ref} is the reference solution and $\mathbf{x}$ is the approximate solution.

4. Numerical test cases

In this section numerical examples are provided to demonstrate that the results remain consistent as a result of grid refinement and that iterations used for estimating stick-slip conditions converge to the correct solution. These examples also show the applicability of the sEFVM for non-faulted continuum media (i.e. FVM) and faulted domains. For non-faulted media, sEFVM reduces to FVM. As such, we perform the study for FVM when no faults and fractures are present. For faulted domains, comparative studies are also carried out to identify the key strengths of the fully-implicit, fully-coupled sEFVM compared with sequentially-coupled, non-iterative and oscillatory EFVM.

4.1. Consistency and order of accuracy verification for pure mechanics in non-faulted/fractured media

Analytical displacement fields (u_x, u_y) for a 2D homogeneous domain, taken from the literature [57], are given as

$$\begin{aligned} u_x &= \quad 10^{-5} \sin\left(\frac{\pi x}{L}\right) \sin\left(\frac{\pi y}{W}\right), \\ u_y &= -10^{-5} \cos\left(\frac{\pi (L-x)}{L}\right) \sin\left(\frac{\pi y}{W}\right), \end{aligned} \tag{29}$$

where L and W are model length and width, both taken equal to 1 m here. Moreover, λ and G are, respectively, 10 GPa and 2.5 GPa. Fig. 3 illustrates the error of the solutions obtained by FVM, i.e. ϵ, for different mesh sizes Δx. Note that $\Delta x = \Delta y$ at all refinement levels. This test confirms the consistency of the FVM implementation, in the absence of faults. The order of accuracy is confirmed to be 2, consistent with the literature [57].

4.2. Benchmark for poromechanics simulations for non-faulted/fractured media: Terzaghi test case

In this test case, complementary to the previously-studied pure mechanics test case, the sEFVM (which again reduces to FVM in the absence of faults) is validated for poromechanics deformation. A porous medium is compressed from the top and constrained from movement in the normal direction on all other sides. Fluid is allowed to drain from the top, while a no-flow sealing condition applies to all other sides. Fig. 4 shows an illustration of this test case, which is named after Terzaghi [64].

A 1×1 m^2 porous medium is considered, for which $E = 1e4$ Pa, $\nu = 0.2$, $k_m/\mu = 1e-4$ m^2/Pa.sec, $b = 1$ and $M = 1e100$ are assigned. Moreover, F is 100 Pa and the time-step size of $\Delta t = 0.001$ sec is taken. The initial pressure in the system is set to be 100 Pa. The computational grid consists of 100×100 cells. Fig. 5 shows the pressure and displacement profiles only across the depth of the domain, since there exists no change along the horizontal direction. Pressure declines with time as fluid drains from the top of the porous medium. Vertical displacement is negative, indicating contraction of the compressed system. The contraction increases with time. It is seen that the numerical and analytical results closely replicate each other. More precisely, as an example, the errors of sEFVM (which again turns to FVM in the absence of faults and fractures) solution at simulation time 0.9 sec are $\epsilon_{u_y} = 1e-3$ for the vertical displacement and $\epsilon_p = 1.6e-3$ for pressure.

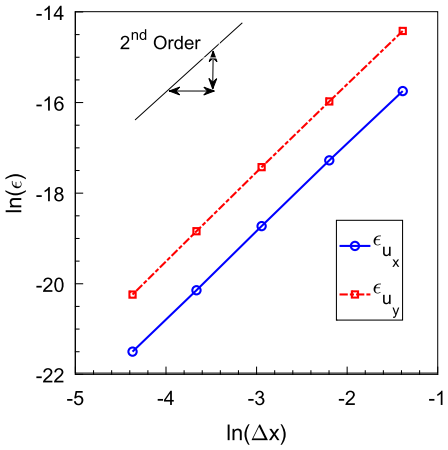

Fig. 3. Second order accuracy of the FVM model.

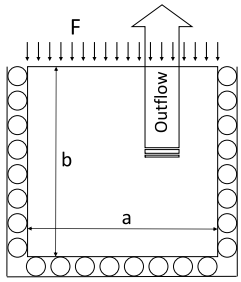

Fig. 4. Illustration of Terzaghi poromechanics test case.

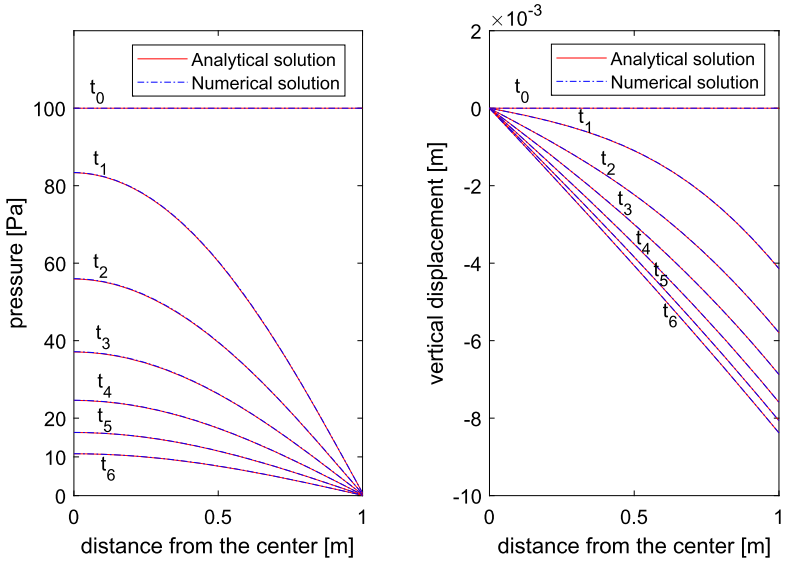

Fig. 5. Pressure (left) and displacement (right) profiles for Terzaghi test case at times t_1 to t_6 with values 0, 0.15, 0.3, 0.45, 0.6, 0.75 and 0.9 sec, respectively.

4.3. Benchmark for poromechanics simulations for non-faulted/fractured media: Mandel test case

In this section the sEFVM numerical model, which will be reduced to FVM due to the absence of faults, is compared with the analytical solution to the Mandel test case. A poroelastic sponge of length $2a$ and width $2b$ is assumed to be open to flow at both ends. This sponge is compressed from the top and from below with force F. The analytical solution for

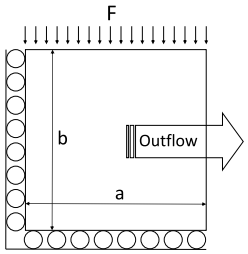

Fig. 6. Mandel problem illustration.

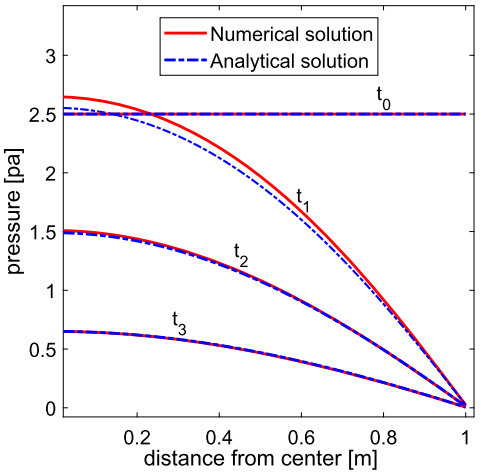

Fig. 7. Pressure profiles for the Mandel test case at times t_0 to t_3 with values 0, 5, 15, 30 sec, respectively.

pressure and displacement distributions is given in [64]. Due to its symmetric geometry, only a quarter of the domain needs to be modeled as illustrated in Fig. 6.

Model dimensions, computational grid resolution, and values of E, ν, k_m/μ, b and M are all taken the same as in the Terzaghi test case. Moreover, F is 5 Pa and the time-step size is $\Delta t = 0.1$ sec. The initial pressure in the system is set to be 2.5 Pa. Fig. 7 shows the pressure profile along the horizontal center-line of the model at different times. This image shows that the pressure drops as fluid flows out of the right side. At smaller times, i.e. $t_1 = 5$ sec, there is a small pressure buildup above initial conditions near the center of the system. This occurs due to the contraction of the drained edges [64]. Fig. 7 also confirms that the solution of the FVM numerical model is close to the analytical solution. More specifically, with the chosen grid resolution and time step size, at $t_4 = 30$ sec, the errors are $\epsilon_p = 6.1e-3$ for pressure, $\epsilon_{u_x} = 3.6e-2$ for displacement along the x axis, and $\epsilon_{u_y} = 5e-3$ for displacement along the y axis.

4.4. Modeling of plane strain subsidence in a heterogeneous depleting gas field

The goal of this section is to compare the numerical FVM poroelastic model with a purely-mechanical FVM model for modeling plane strain subsidence in a heterogeneous setting. It is expected that the solution of the poroelastic model asymptotically reaches the mechanical one at long times. The surface subsidence is studied in a gas field in the Adriatic basin neighboring Italy. The geometry of Fig. 8 is conceptualized based on published data [68]. Two methods were used for studying surface subsidence. In the first, the system is modeled dynamically assuming flow inside the porous reservoir. This reservoir is encapsulated by an elastic non-porous medium. In the second approach, the system is entirely impermeable and elastic. For this setup, a force equivalent to the pressure depletion of the dynamic model is applied to the outer boundaries of the assumed reservoir at each time-step.

The reservoir is stationary (zero displacements) at all boundaries except for the top free surface. The porous region has no-flow boundaries. The computational grid consists of 50×150 cells, with finer mesh vertically to capture the thin reservoir. A single gas producer is considered for depletion. The mobility in the horizontal direction is $k_{m,x}/\mu = 8e-10$ m^2/Pa.sec. The vertical to horizontal permeability is $k_{m,y}/k_{m,x} = 0.1$. Value of Poison ratio is $\nu = 0.3$ and $b = 1$. An empirical correlation is used for the Young's modulus (E) in this field as given by [69].

$$E = \frac{(1-2\nu)(1+\nu)}{(1-\nu)c_M}, \tag{30}$$

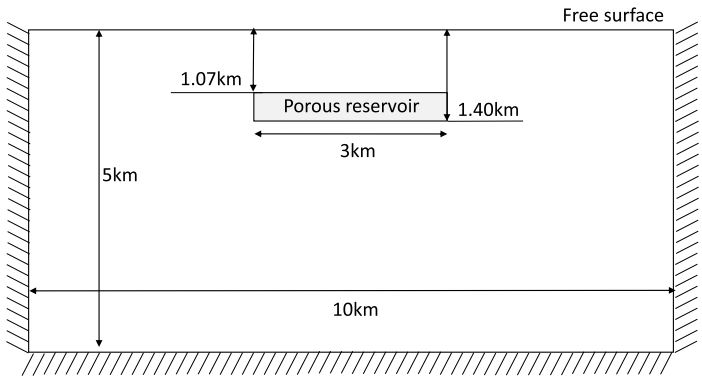

Fig. 8. Illustration for modeling plane strain subsidence.

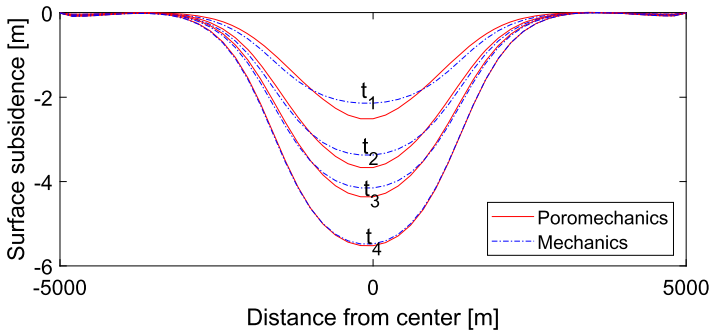

Fig. 9. Comparison of evolution of surface subsidence in a depleting gas field as predicted using static and poroelastic FVM models at t_1 to t_4 corresponding to 6, 18, 30 and 90 months.

where c_M is the vertical compressibility in $bars^{-1}$ found as a function of depth (z, in meters) according to [69] as

$$c_M = 0.01241 \mid 0.1\, z - 0.12218\, z^{1.0766} \mid^{-1.1342}. \tag{31}$$

Values of E and ν are used for determining Lame constants used in Eq. (17) according to available conversion formulae [64]. The Biot modulus (M, which appears in Eq. (1)) is calculated as [70]

$$\frac{1}{M} = \frac{\phi}{K_{fl}} + \frac{b-\phi}{K_s}, \tag{32}$$

where K_{fl} and K_s are fluid and solid moduli taken as 0.02 and 1e100 GPa, respectively. The ϕ is porosity (as a fraction) calculated as a function of depth (z, in meters) as [71]

$$\phi = -0.005\, log(z) + 0.3. \tag{33}$$

Fig. 9 shows the evolution of surface subsidence for the studied problem. The static and dynamic results are plotted at various simulation times. It can be seen that both methods converge to the same solution at late times. This is an expected outcome. Errors are quantified according to Eq. (28). At simulation time $t = 500t_c$, the errors are $\epsilon_{u_y} = 1.26e-2$ and $\epsilon_{u_x} = 1.53e-2$ for displacement fields. The error for surface subsidence is $5.0e-3$.

4.5. Faulted reservoir in an infinite domain

A finite reservoir is assumed in an infinite domain. A vertical fault with an initial offset is present in the middle of the reservoir. The fault is fully permeable but does not transmit fluid pressure above the top or below the bottom of the reservoir. The setup is shown in Fig. 10. Analytical solutions for production/injection-induced displacements, stresses and strains for this system are given by [72]. Here, we compare our numerical model with the analytical solutions for the shear stress along the fault.

Elastic parameters are $G = 6.5$ GPa and $\nu = 0.15$. The fault surfaces are frictionless. Values of a and b in Fig. 10 are 75 and 150 meters, respectively. In the analytical solution, the reservoir stretches throughout the entire horizontal extent of the system. To approximate such infinite boundaries, the external medium in the numerical set up is assumed 10 times larger than the reservoir thickness (i.e. 2250×2250 meters). Roller boundary conditions are considered on all external boundaries.

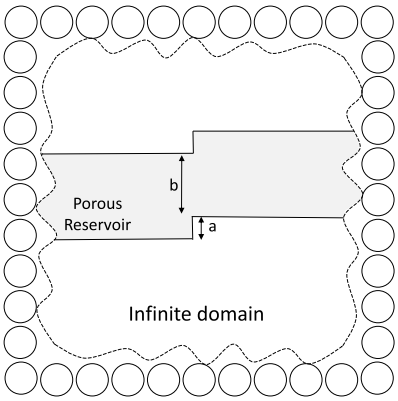

Fig. 10. Schematic of a faulted reservoir in an infinite domain.

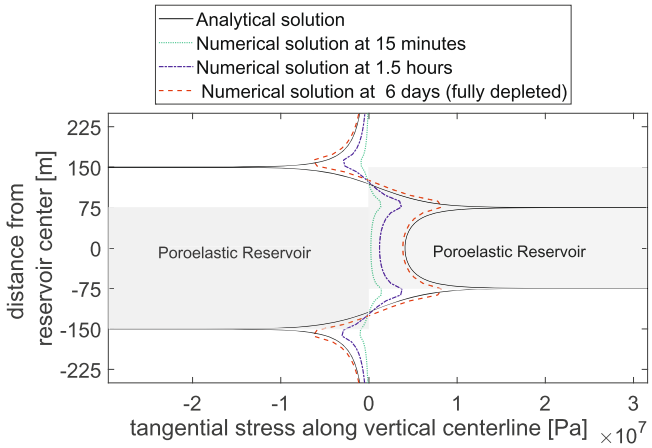

Fig. 11. Shear stress profile across the vertical center-line in an infinite faulted reservoir.

The reservoir boundaries are impermeable. The reservoir is depleted via a single production well placed centrally in the reservoir. This well produces at a constant draw down pressure of ΔP = -25 MPa. The computational grid consists of 200 × 200 cells. The numerical results were obtained by considering different orders for the time-step (1 minute, 1 hour and 1 day).

The shear stress is plotted along the depth of the reservoir at the location of the fault. Fig. 11 shows the results of the dynamic FVM model at various time-steps and the analytical solution based on equations in [72]. The stress profile shows 2 minima and 2 maxima. These extrema correspond to the 4 edges of the displaced reservoir sections. The numerical solution approaches the analytical solution at full depletion, which is seen after approximately 6 days, although the finite grid resolution results in smoothed extrema instead of the peaks of infinite magnitude as observed in the analytical solution.

4.6. Elastic faulted model

The analytical solution for the slip profile in the faulted, unbounded and elastic block of Fig. 12 is found as [73]

$$s\,(L_x) \;=\; \frac{2(1-\nu^2)\,\tau_c}{E}\sqrt{L_f^2-(x-L_f)^2}, \tag{34}$$

where L_x is the location along the fault and L_f is the fault length. θ is the friction angle defined as [73]

$$|\,\tau\,| = -\tan\theta\,\sigma_n, \tag{35}$$

and τ_c is defined as

$$\tau_c = \sigma\,\sin\alpha\,\Big(\cos\alpha - \sin\alpha\,\tan\theta\Big), \tag{36}$$

where α is the angle of the fault with the negative direction of the horizontal axis.

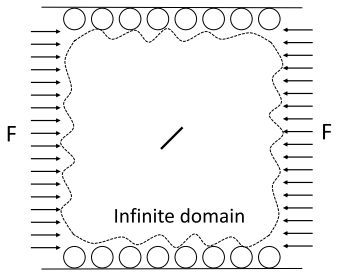

Fig. 12. Illustration for the infinite, elastic faulted system under compression.

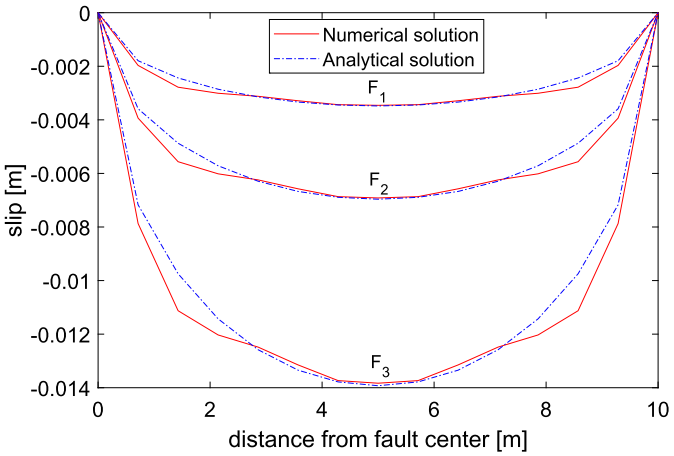

Fig. 13. Comparison of analytical solutions with numerical solutions of EFVM for the slip profile in a infinite faulted domain under compression loads of F_1 to F_3 equal to 50, 100 and 200 MPa.

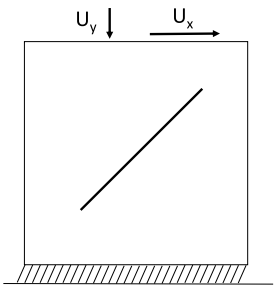

Fig. 14. Illustration for faulted test case with surface displacements.

A 100×100 m^2 square is considered. There is a 10 meter fault at the center of the block with $\theta = 20$ degrees. Force F compresses the horizontal sides of the block. Top and bottom are constrained from normal displacement to simulate an infinite vertical domain. Values of $E = 7e10$ Pa, $\nu = 0.2$ and $\alpha = 30$ degrees are assigned to the model. The computational grid consists of 100×100 cells. The slip profiles from the analytical solution and EFVM are shown in Fig. 13 for three different values of F of 50, 100 and 200 MPa. These results show good agreement between EFVM and analytical solutions. The slip increases with increased applied force.

4.7. Test case with oscillatory behavior and the use of sEFVM

EFVM method can produce non-smooth profiles for the slip and stress fields. As an example, a 1×1 m^2 elastic domain is considered. The top and the bottom surfaces are subject to a Dirichlet displacement vector (u_x, u_y) of $(0, 0)$ and $(0.05, 0.005)$ meters, respectively. The east and west boundaries are subject to free stress conditions. A fault is defined with a length of 0.4 m, located centrally, having an angle of α with respect to the horizontal axis. Lame parameters are both chosen equal to 1 Pa. The friction coefficient is set to be 0.85. The setup is shown in Fig. 14.

The slip profile for the case of a horizontal fault (i.e., $\theta = 0$) is shown in Fig. 15a. For this case, the slip profile is smooth and in good agreement with results of the Porepy simulator [74]. The order of accuracy for slip is determined by altering

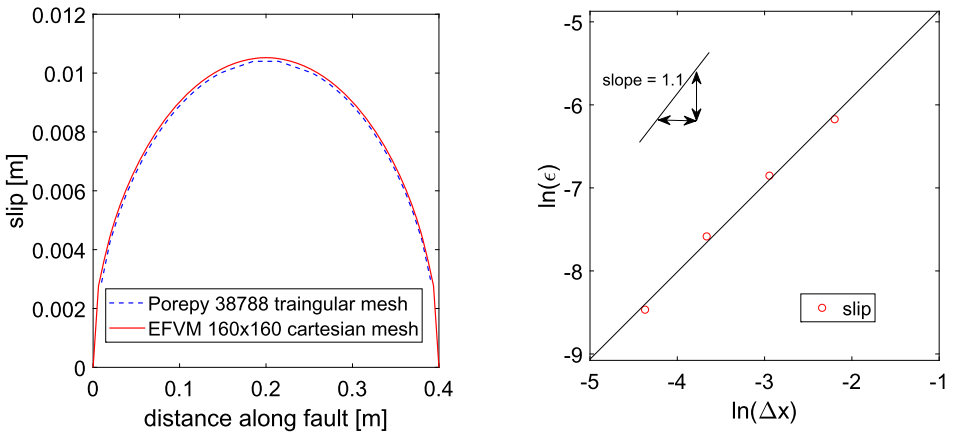

Fig. 15. EFVM slip profile (left) and the order of accuracy of slip (right) for a block with surface displacement and a horizontal fault.

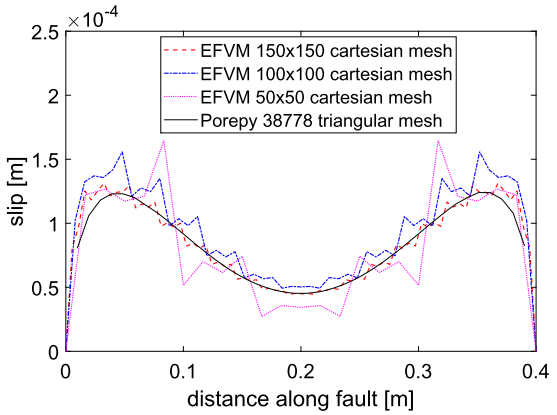

Fig. 16. Convergent oscillatory solution of EFVM for the slip profile for a fault inclined at 18 degrees.

the computational grid from 10×10 to 160×160. The error is calculated using Eq. (28) with respect to the most refined mesh (i.e., 160×160) and plotted in Fig. 15b. This figure shows that the slip profile converges linearly to the solution.

However, the smoothness of the slip profile is not always guaranteed. The same setup is modeled by rotating the fault to an angle of $\alpha = 18$ degrees. The slip profile is shown in Fig. 16. For this example, the slip profile takes a saddle form, and the fully-implicit EFVM results are non-smooth. Note that the EFVM results, even though being non-smooth, are fully converged for the state of slip-stick at each fault node.

We elaborate on a few points. First, we see in Fig. 16 that the magnitude of oscillations decays as the mesh gets finer, and that the slip function remains convergent in spite of oscillatory behavior. However, oscillations can pose a significant challenge as the stress field becomes also non-smooth. Notice that the stress field is used to determine slip-stick conditions of the fault. When the fault is critically stressed, the oscillations can potentially result in an incorrect determination of slipping nodes. Therefore, it is crucial to systematically resolve the oscillations within the stress field.

To resolve this challenge, and guarantee smoothness of the results, we complement EFVM with a smoothing procedure, and refer to it as sEFVM. A polynomial fit to the oscillating curve is used to capture the behavior without oscillations. It is found that this fitted polynomial is in close agreement with the expected results. For the studied example, this is shown in Fig. 17 for stress and slip. The fit is in good agreement with results of Porepy and the solution of EFVM on a finer mesh.

The smoothed solutions presented in Fig. 17 for the stress and slip profiles are

$$\tau\ (L_x) = c_1 L_x^2 + c_2 L_x + c_3, \tag{37a}$$

$$s\ (L_x) = d_1 L_x^4 + d_2 L_x^3 + d_3 L_x^2 + d_4 L_x + d_5, \tag{37b}$$

where L_x is the distance from the beginning of the fault in meters (i.e., the tip with minimum x and y values). Values of c_1 to c_3 are found as -0.1508 Pa/m^2, 0.06031 Pa/m and 0.02948 Pa, respectively. Values of d_1 to d_5 are found as -0.1821 m^{-3}, 0.1457 m^{-2}, -0.03589 m^{-1}, 0.002701 and $6.003e-5$ m, respectively. The norm of residuals for stress and slip are $3.8e-3$ Pa and $1.1e-4$ m, respectively. The small norm values indicate a good fit.

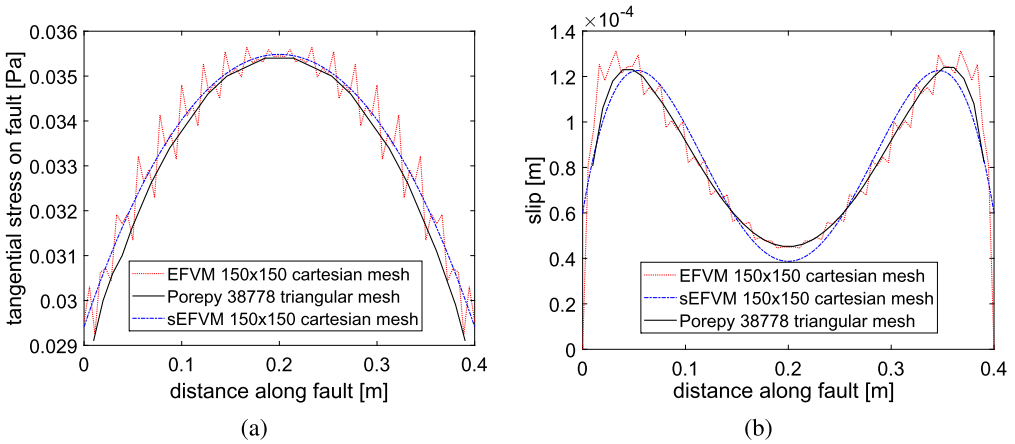

Fig. 17. Post-processing of the stress (left) and slip profile (right) in sEFVM for the example of a fault inclined at 18 degrees.

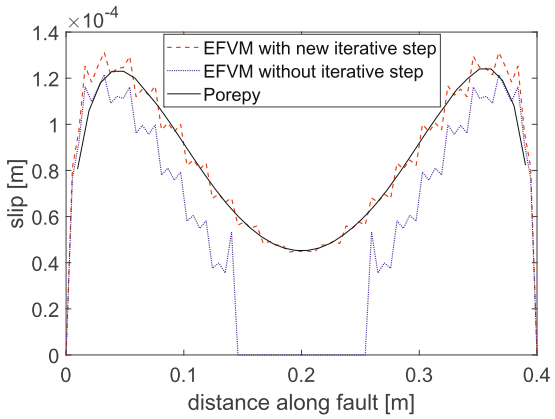

Fig. 18. Demonstration of the role of the new iterative step in sEFVM for the example of a fault inclined at 18 degrees in the block with surface displacement.

Note that the EFVM oscillations are due to the misaligned faults and the embedded grid cells. This is why for horizontal and vertical fractures/faults the oscillations do not occur as shown in Fig. 15b. It is emphasized that the stress at the location of the fracture/fault is calculated based on the values of displacement of the hosting structured grid and the value of the slip and the location of the fracture/fault node. When following the path of the fracture/fault, the stress values change from grid to grid. When plotting the stress along the fracture/fault, these changes can result in oscillatory profiles along the direction of the embedded fracture/fault. The magnitude of the oscillations depends entirely on the stress distribution at the location of the fracture/fault and how the fracture/fault element is cutting through the matrix grids which in turn depends on the resolution as shown in Fig. 16. Depending on the situation, oscillations can be pronounced or visibly undetectable.

For most problems, EFVM is found to be smooth. But when oscillations do arise, the proposed procedure leading to sEFVM guarantees smooth solutions for all faults. This is crucial for practical cases which typically involve challenging fault geometries and orientations.

As explained in Algorithm 1, another important advancement of the proposed fully-coupled fully-implicit sEFVM is that the state of slip-stick is found implicitly based on the updated state of the stress. One can observe severe errors in the fault slip predictions, if this important feature is neglected, as, e.g., observed in references [55,56] where the stress from the previous time step is used to indicate the slip-stick state of fault nodes. Fig. 18 illustrates this important aspect, by presenting the slip profile when no iterations are employed to indicate the slip-stick state.

4.8. Heavily-faulted poroelastic model

A conceptual model is considered with dimensions of 30×50 km^2. Values of $\nu = 0.2$, $b = 1$ and $\phi = 0.2$ are assigned to the model. The system is heavily-faulted with 29 impermeable faults, some of which can get very close to each other. The model consists of a poroelastic saturated reservoir surrounded by an impermeable elastic external medium. A production well is placed centrally in the porous reservoir region. The initial reservoir pressure and production well bottom-hole

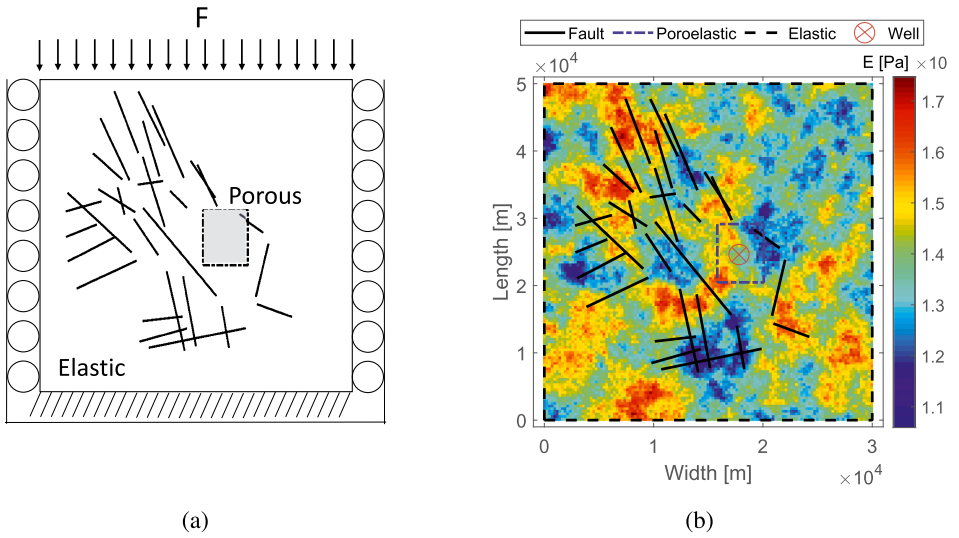

Fig. 19. Schematic (left) and heterogeneous map for the Young modulus (right) of a heavily faulted poroelastic model.

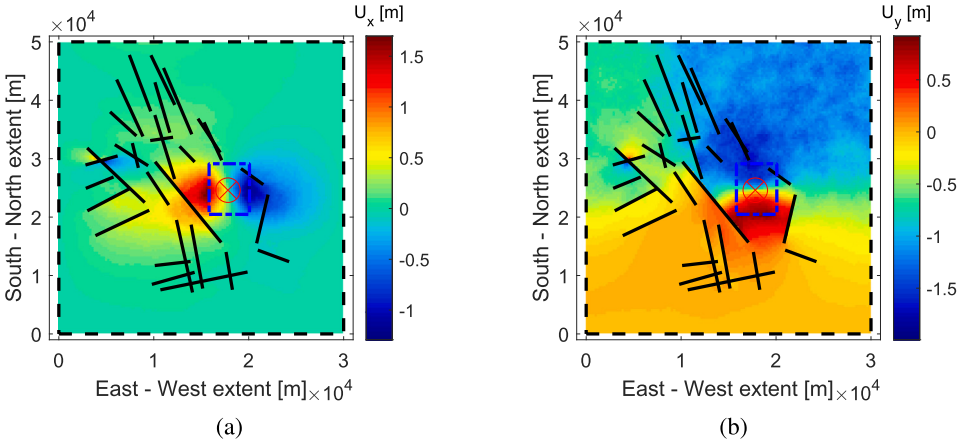

Fig. 20. Horizontal (Fig. 20a) and vertical displacement fields (Fig. 20b) in a heavily faulted poroelastic model.

pressures are 150 MPa and 100 MPa, respectively. Mobility is $1e-6$ m^2/Pa.sec. The friction coefficient for all faults is set to be 0.6. The computational grid consists of 128×128 cells, and the time step size is 1.5 hours. A force per length of 1 kPa/m is applied at the top boundary. The bottom boundary is stationary. Horizontal boundaries are constrained from normal displacement as shown in Fig. 19a.

Fig. 20 shows the displacement field for the test case after 15 hours. Both horizontal and vertical displacements show the highest deformation inside and in the vicinity of the porous reservoir domain. The effect of the heterogeneous E field is clearly seen in the vertical displacement profile, resulting in heterogeneous displacement patterns.

The Von Mises stress, i.e. σ_{VM}, and pressure maps are shown in Fig. 21. According to the stress map, the maximum stress is observed inside the poroelastic region. The pressure profile reflects the depletion inside the porous region. One fault which intersects with the reservoir at the top right boundary has influenced depletion in that region. It is worth mentioning that in this test case, no smoothing was required as the EFVM results were non-oscillatory.

5. Conclusions

The finite volume method was used in this study for modeling poroelastic media in the presence of faults and fractures. In the absence of fractures and faults, the method reduces to the fully-coupled fully-implicit FVM, which was confirmed to be second order accurate for pure mechanical deformation. Several studies were performed to investigate the consistency and accuracy of the method for analytical and well-established test cases such as Mandel and Terzaghi. These also include plane strain subsidence, in which a fully-coupled poromechanics model was compared against one-way-coupled pure me-

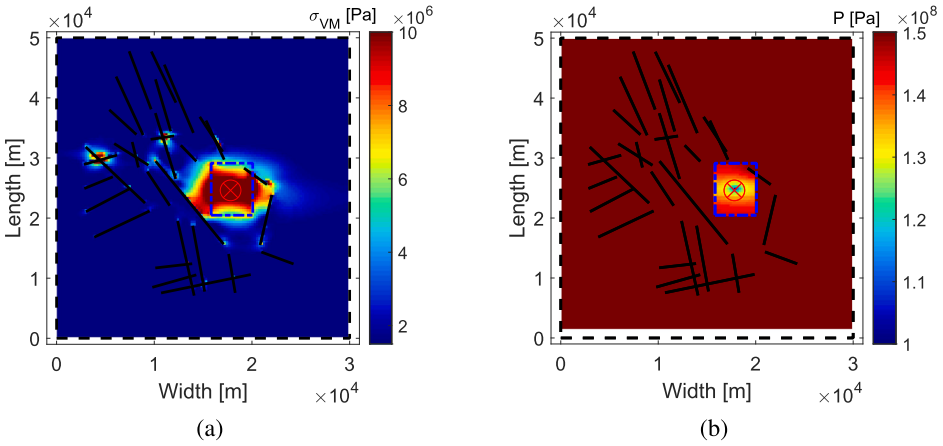

Fig. 21. Von Mises stress (left) and pressure map (right) in a heavily faulted poroelastic model.

chanics in which pore-pressure drop was imposed as boundary condition. It was shown that while the steady-state solutions of these two approaches match, the transient solutions do not.

In the presence of faults, the developed sEFVM was investigated for several test cases including benchmark studies against analytical solutions. It was shown that the fully-implicit and fully-coupled nature of the sEFVM was essential to accurately estimate the slip-stick state of fault nodes consistent with the state-of-the-stress. In addition, the possible occurrence of fluctuating stress and slip fields within the EFVM method, as observed in the literature, was eliminated by a novel smoothed procedure, resulting in a smoothed EFVM method (sEFVM).

It was demonstrated that the sEFVM can effectively cope with test cases in which many faults coexist in a heterogeneous domain. The use of independent grids for the discontinuities, i.e. faults and fractures, and their hosting rock cells is an advantage of the method for heavily faulted/fractured systems.

CRediT authorship contribution statement

Sara Shokrollahzadeh Behbahani: Conceptualization, Methodology, Software, Implementation, Results, Writing – original draft.

Hadi Hajibeygi: Conceptualization, Methodology, Writing - review & editing, Supervision.

Denis Voskov: Conceptualization, Methodology, Writing - review & editing, Supervision.

Jan Dirk Jansen: Conceptualization, Methodology, Writing - review & editing, Supervision.

Declaration of competing interest

The authors declare that they have no known competing financial interests or personal relationships that could have appeared to influence the work reported in this paper.

Acknowledgement

This publication is part of the project ‘Science4Steer: a scientific basis for production and reinjection strategies to minimize induced seismicity in Dutch gas fields’ (with project number DEEP.NL.2018.046) of the research programme ‘DeepNL’ which is financed by the Dutch Research Council (NWO). Hadi Hajibeygi was sponsored by NWO, under the Innovational Research Incentives Scheme Vidi, project “ADMIRE”, grant no. 17509.

Appendix A

In this section, examples of analytical derivation of the terms in Eq. (18) are provided. The integral in this equation contains derivatives of displacement which are also found analytically based on definitions given in Eq. (19). For example

$$\frac{\partial u_x}{\partial y} = \frac{\partial N_1(x,y)}{\partial y} u_{x,1} + \frac{\partial N_2(x,y)}{\partial y} u_{x,2} + \frac{\partial N_3(x,y)}{\partial y} u_{x,3} + \frac{\partial N_4(x,y)}{\partial y} u_{x,4} + \frac{\partial W(x,y)}{\partial y} st_x. \tag{38}$$

The numbering scheme is shown in Fig. 1. Next, derivatives in Eq. (38) are calculated. For example

$$\frac{\partial N_1(x,y)}{\partial y} = (\frac{-1}{\Delta y})(1 - \frac{x}{\Delta x}), \tag{39}$$

and for the multiplier of slip

$$\frac{\partial W(x,y)}{\partial x} = \frac{\partial N_1(x,y)}{\partial x}[H(f(x,y)) - H(f(x_1,y_1))] + \frac{\partial N_2(x,y)}{\partial x}[H(f(x,y)) - H(f(x_2,y_2))] + \frac{\partial N_3(x,y)}{\partial x}[H(f(x,y)) - H(f(x_3,y_3))] + \frac{\partial N_4(x,y)}{\partial x}[H(f(x,y)) - H(f(x_4,y_4))],$$

where the values of $\left[H(f(x,y)) - H\left(f\left(x_i,y_j\right)\right)\right]$ are found numerically based on the local coordinates of corner points (x_i and y_i) at any location x and y. For each grid cell, this location is the coordinate of the fault node.

Next, the integral in Eq. (18) is determined. This integral is calculated analytically at boundary segments A_1 to A_8 shown in Fig. 1. The range of integrals are from $\frac{-\Delta x}{2}$ to $\frac{\Delta x}{2}$ and $\frac{-\Delta y}{2}$ to $\frac{\Delta y}{2}$ for x and y, respectively. One example is provided for an integral over section A_1 as

$$\int_{A_1} \frac{\partial u_x}{\partial y} dx = [(\frac{-u_{x,1}}{8} - \frac{-3u_{x,2}}{8} + \frac{3u_{x,3}}{8} + \frac{u_{x,4}}{8}) + (\frac{-H_1}{8} - \frac{-3H_2}{8} + \frac{3H_3}{8} + \frac{1H_4}{8})st_x]\frac{\Delta x}{\Delta y}. \tag{40}$$

Other integrals are obtained similarly. The multipliers for u_1 to u_4 are used to find components of J_{uu} in Eq. (27). The coefficients for s in above integral give J_{us}.

For J_{up_m}, the following term from Eq. (18) is integrated as

$$\int_{\partial\Omega_u} -bp_m dy = \frac{-b\Delta y}{2}((p_{m_4} + p_{m_1}) - (p_{m_3} + p_{m_2})). \tag{41}$$

The numbering scheme is shown in Fig. 1. The momentum balance equation is not assumed to be affected by fault pressure, therefore J_{up_f} is an array of zeros.

References

[1] M.D. Zoback, Reservoir Geomechanics, Cambridge University Press, 2010.
[2] P.J. Phillips, M.F. Wheeler, A coupling of mixed and continuous Galerkin finite element methods for poroelasticity I: the continuous in time case, Comput. Geosci. 11 (2) (2007) 131.
[3] Z.P. Bažant, M. Salviato, V.T. Chau, H. Viswanathan, A. Zubelewicz, Why fracking works, J. Appl. Mech. 81 (10) (2014).
[4] R.A. Morton, J.C. Bernier, J.A. Barras, Evidence of regional subsidence and associated interior wetland loss induced by hydrocarbon production, Gulf Coast region, USA, Environ. Geol. 50 (2) (2006) 261.
[5] M. Grant, Geothermal Reservoir Engineering, Elsevier, 2013.
[6] K.S. Lackner, A guide to co2 sequestration, Science 300 (5626) (2003) 1677–1678.
[7] S. Bauer, C. Beyer, F. Dethlefsen, P. Dietrich, R. Duttmann, M. Ebert, V. Feeser, U. Görke, R. Köber, O. Kolditz, et al., Impacts of the use of the geological subsurface for energy storage: an investigation concept, Environ. Earth Sci. 70 (8) (2013) 3935–3943.
[8] F. Zhang, P. Zhao, M. Niu, J. Maddy, The survey of key technologies in hydrogen energy storage, Int. J. Hydrog. Energy 41 (33) (2016) 14535–14552.
[9] K.R. Kumar, H. Hajibeygi, Multiscale simulation of inelastic creep deformation for geological rocks, J. Comput. Phys. 440 (2021) 110439.
[10] N.R. Council, et al., Induced Seismicity Potential in Energy Technologies, National Academies Press, 2013.
[11] R. Van Eijs, F. Mulders, M. Nepveu, C. Kenter, B. Scheffers, Correlation between hydrocarbon reservoir properties and induced seismicity in the Netherlands, Eng. Geol. 84 (3–4) (2006) 99–111.
[12] NAM, Nam ambient aware and participating in society, https://www.nam.nl/english-information.html.
[13] K. Park, Stabilization of partitioned solution procedure for pore fluid-soil interaction analysis, Int. J. Numer. Methods Eng. 19 (11) (1983) 1669–1673.
[14] O. Zienkiewicz, D. Paul, A. Chan, Unconditionally stable staggered solution procedure for soil-pore fluid interaction problems, Int. J. Numer. Methods Eng. 26 (5) (1988) 1039–1055.
[15] J. Kim, H.A. Tchelepi, R. Juanes, Stability and convergence of sequential methods for coupled flow and geomechanics: fixed-stress and fixed-strain splits, Comput. Methods Appl. Mech. Eng. 200 (13–16) (2011) 1591–1606.
[16] R.W. Lewis, R.W. Lewis, B. Schrefler, The Finite Element Method in the Static and Dynamic Deformation and Consolidation of Porous Media, John Wiley & Sons, 1998.
[17] J.W. Both, K. Kumar, J.M. Nordbotten, F.A. Radu, The gradient flow structures of thermo-poro-visco-elastic processes in porous media, arXiv preprint arXiv:1907.03134, 2019.
[18] J. Byerlee, Friction of rocks, in: Rock Friction and Earthquake Prediction, Springer, 1978, pp. 615–626.
[19] M. Nejati, A. Paluszny, R.W. Zimmerman, A finite element framework for modeling internal frictional contact in three-dimensional fractured media using unstructured tetrahedral meshes, Comput. Methods Appl. Mech. Eng. 306 (2016) 123–150.
[20] Y. Ida, Cohesive force across the tip of a longitudinal-shear crack and Griffith's specific surface energy, J. Geophys. Res. 77 (20) (1972) 3796–3805.
[21] C.H. Scholz, Earthquakes and friction laws, Nature 391 (6662) (1998) 37–42.
[22] J.H. Dieterich, Modeling of rock friction: 1. Experimental results and constitutive equations, J. Geophys. Res., Solid Earth 84 (B5) (1979) 2161–2168.
[23] A. Ruina, Slip instability and state variable friction laws, J. Geophys. Res., Solid Earth 88 (B12) (1983) 10359–10370.
[24] R.P. Pijnenburg, C.J. Spiers, Microphysics of inelastic deformation in reservoir sandstones from the seismogenic center of the Groningen gas field, Rock Mech. Rock Eng. 53 (12) (2020) 5301–5328.
[25] A. Niemeijer, C. Spiers, Velocity dependence of strength and healing behaviour in simulated phyllosilicate-bearing fault gouge, Tectonophysics 427 (1–4) (2006) 231–253.
[26] A. Niemeijer, C. Spiers, A microphysical model for strong velocity weakening in phyllosilicate-bearing fault gouges, J. Geophys. Res., Solid Earth 112 (B10) (2007).

[27] J. Chen, C.J. Spiers, Rate and state frictional and healing behavior of carbonate fault gouge explained using microphysical model, J. Geophys. Res., Solid Earth 121 (12) (2016) 8642–8665.
[28] Z. Reches, Dynamic frictional slip along rock faults, J. Tribol. 142 (12) (2020).
[29] M. Van den Ende, J. Chen, J.-P. Ampuero, A. Niemeijer, A comparison between rate-and-state friction and microphysical models, based on numerical simulations of fault slip, Tectonophysics 733 (2018) 273–295.
[30] E. Ucar, E. Keilegavlen, I. Berre, J. Nordbotten, A finite-volume discretization for deformation of fractured media, Comput. Geosci. 22 (2018) 993–1007, https://doi.org/10.1007/s10596-018-9734-8.
[31] B. Baliga, T. Pham, S. Patankar, Solution of some two-dimensional incompressible fluid flow and heat transfer problems, using a control volume finite-element method, Numer. Heat Transf. 6 (3) (1983) 263–282.
[32] F. Gaspar, F. Lisbona, P. Vabishchevich, Staggered grid discretizations for the quasi-static Biot's consolidation problem, Appl. Numer. Math. 56 (6) (2006) 888–898.
[33] S. Salimzadeh, A. Paluszny, H.M. Nick, R.W. Zimmerman, A three-dimensional coupled thermo-hydro-mechanical model for deformable fractured geothermal systems, Geothermics 71 (2018) 212–224.
[34] F. Gaspar, F. Lisbona, P. Vabishchevich, A finite difference analysis of Biot's consolidation model, Appl. Numer. Math. 44 (4) (2003) 487–506.
[35] M. Vinokur, An analysis of finite-difference and finite-volume formulations of conservation laws, J. Comput. Phys. 81 (1) (1989) 1–52.
[36] J. Peiró, S. Sherwin, Finite difference, finite element and finite volume methods for partial differential equations, in: Handbook of Materials Modeling, Springer, 2005, pp. 2415–2446.
[37] E. Stein, History of the finite element method–mathematics meets mechanics–part I: engineering developments, in: The History of Theoretical, Material and Computational Mechanics-Mathematics Meets Mechanics and Engineering, Springer, 2014, pp. 399–442.
[38] H. Matthies, G. Strang, The solution of nonlinear finite element equations, Int. J. Numer. Methods Eng. 14 (11) (1979) 1613–1626.
[39] T.J. Hughes, The Finite Element Method: Linear Static and Dynamic Finite Element Analysis, Courier Corporation, 2012.
[40] S. Salimzadeh, M. Grandahl, M. Medetbekova, H. Nick, A novel radial jet drilling stimulation technique for enhancing heat recovery from fractured geothermal reservoirs, Renew. Energy 139 (2019) 395–409.
[41] M. Rashid, The arbitrary local mesh replacement method: an alternative to remeshing for crack propagation analysis, Comput. Methods Appl. Mech. Eng. 154 (1–2) (1998) 133–150.
[42] S. Bosma, H. Hajibeygi, M. Tene, H.A. Tchelepi, Multiscale finite volume method for discrete fracture modeling on unstructured grids (ms-dfm), J. Comput. Phys. 351 (2017) 145–164.
[43] L. Li, D. Voskov, A novel hybrid model for multiphase flow in complex multi-scale fractured systems, J. Pet. Sci. Eng. 203 (2021) 108657.
[44] T.T. Garipov, M. Karimi-Fard, H.A. Tchelepi, Discrete fracture model for coupled flow and geomechanics, Comput. Geosci. 20 (1) (2016) 149–160, https://doi.org/10.1007/s10596-015-9554-z.
[45] J.M. Nordbotten, Cell-centered finite volume discretizations for deformable porous media, Int. J. Numer. Methods Eng. 100 (6) (2014) 399–418.
[46] K.M. Terekhov, Cell-centered finite-volume method for heterogeneous anisotropic poromechanics problem, J. Comput. Appl. Math. 365 (2020) 112357.
[47] A. Novikov, D. Voskov, M. Khait, H. Hajibeygi, J. Jansen, A collocated finite volume scheme for high-performance simulation of induced seismicity in geo-energy applications, in: SPE Reservoir Simulation Conference, OnePetro, 2021.
[48] L. Li, S.H. Lee, et al., Efficient field-scale simulation of black oil in a naturally fractured reservoir through discrete fracture networks and homogenized media, SPE Reserv. Eval. Eng. 11 (04) (2008) 750–758.
[49] R. Löhner, J.R. Cebral, F.E. Camelli, S. Appanaboyina, J.D. Baum, E.L. Mestreau, O.A. Soto, Adaptive embedded and immersed unstructured grid techniques, Comput. Methods Appl. Mech. Eng. 197 (25–28) (2008) 2173–2197.
[50] H. Hajibeygi, D. Karvounis, P. Jenny, A hierarchical fracture model for the iterative multiscale finite volume method, J. Comput. Phys. 230 (24) (2011) 8729–8743.
[51] M. HosseiniMehr, M. Cusini, C. Vuik, H. Hajibeygi, Algebraic dynamic multilevel method for embedded discrete fracture model (f-ADM), J. Comput. Phys. 373 (2018) 324–345, https://doi.org/10.1016/j.jcp.2018.06.075.
[52] T. Belytschko, N. Moës, S. Usui, C. Parimi, Arbitrary discontinuities in finite elements, Int. J. Numer. Methods Eng. 50 (4) (2001) 993–1013.
[53] A. Fumagalli, A. Scotti, An efficient xfem approximation of Darcy flows in arbitrarily fractured porous media, Oil Gas Sci. Technol. 69 (4) (2014) 555–564.
[54] F. Xu, H. Hajibeygi, L.J. Sluys, Multiscale extended finite element method for deformable fractured porous media, J. Comput. Phys. 436 (2021) 110287.
[55] R. Deb, P. Jenny, Finite volume-based modeling of flow-induced shear failure along fracture manifolds, Int. J. Numer. Anal. Methods Geomech. 41 (18) (2017) 1922–1942.
[56] R. Deb, P. Jenny, Modeling of shear failure in fractured reservoirs with a porous matrix, Comput. Geosci. 21 (5–6) (2017) 1119–1134.
[57] I. Sokolova, M.G. Bastisya, H. Hajibeygi, Multiscale finite volume method for finite-volume-based simulation of poroelasticity, J. Comput. Phys. 379 (2019) 309–324.
[58] B. Flemisch, I. Berre, W. Boon, A. Fumagalli, N. Schwenck, A. Scotti, I. Stefansson, A. Tatomir, Benchmarks for single-phase flow in fractured porous media, Adv. Water Resour. 111 (2018) 239–258.
[59] T. Li, D. Han, F. Yang, B. Yu, D. Sun, J. Wei, A comparative study on simulating flow-induced fracture deformation in subsurface media by means of extended fem and fvm, Oil Gas Sci. Technol. 75 (2020) 41.
[60] P. Segall, J.-R. Grasso, A. Mossop, Poroelastic stressing and induced seismicity near the lacq gas field, southwestern France, J. Geophys. Res., Solid Earth 99 (B8) (1994) 15423–15438.
[61] T.T. Garipov, P. Tomin, R. Rin, D.V. Voskov, H.A. Tchelepi, Unified thermo-compositional-mechanical framework for reservoir simulation, Comput. Geosci. 22 (4) (2018) 1039–1057.
[62] M. Tene, S.B. Bosma, M.S. Al Kobaisi, H. Hajibeygi, Projection-based embedded discrete fracture model (pedfm), Adv. Water Resour. 105 (2017) 205–216.
[63] M.W. McClure, R.N. Horne, Investigation of injection-induced seismicity using a coupled fluid flow and rate/state friction model, Geophysics 76 (6) (2011) WC181–WC198.
[64] H.F. Wang, Theory of Linear Poroelasticity with Applications to Geomechanics and Hydrogeology, vol. 2, Princeton University Press, 2000.
[65] T. Barth, R. Herbin, M. Ohlberger, Finite volume methods: foundation and analysis, in: Encyclopedia of Computational Mechanics, second edition, 2018, pp. 1–60.
[66] J.C. Simo, J. Oliver, F. Armero, An analysis of strong discontinuities induced by strain-softening in rate-independent inelastic solids, Comput. Mech. 12 (5) (1993) 277–296.
[67] C.L. Lawson, R.J. Hanson, Solving Least Squares Problems, SIAM, 1995.
[68] D. Baú, M. Ferronato, G. Gambolati, P. Teatini, Land subsidence spreading factor of the northern Adriatic gas fields, Italy, Int. J. Geomech. 1 (4) (2001) 459–475.
[69] N. Castelletto, H. Hajibeygi, H.A. Tchelepi, Multiscale finite-element method for linear elastic geomechanics, J. Comput. Phys. 331 (2017) 337–356.
[70] B.H. Russell, K. Hedlin, F.J. Hilterman, L.R. Lines, Fluid-property discrimination with avo: a Biot-gassmann perspective, Geophysics V (1) (2003) 29–39.
[71] D. Bau, G. Gambolati, P. Teatini, Residual land subsidence over depleted gas fields in the northern Adriatic basin, Environ. Eng. Geosci. V (4) (1999) 389–405.

[72] J.D. Jansen, P. Singhal, F. Vossepoel, Insights from closed-form expressions for injection- and production-induced stresses in displaced faults, J. Geophys. Res., Solid Earth 124 (7) (2019) 7193–7212.
[73] A.-V. Phan, J. Napier, L. Gray, T. Kaplan, Symmetric-Galerkin bem simulation of fracture with frictional contact, Int. J. Numer. Methods Eng. 57 (6) (2003) 835–851.
[74] E. Keilegavlen, R. Berge, A. Fumagalli, M. Starnoni, I. Stefansson, J. Varela, I. Berre, Porepy: an open-source software for simulation of multiphysics processes in fractured porous media, Comput. Geosci. 25 (1) (2021) 243–265.